Energy &
Environmental
Science

ROYAL SOCIETY
OF CHEMISTRY

PAPER

View Article Online
View Journal | View Issue

Check for updates

Cite this: *Energy Environ. Sci.*, 2024, **17**, 3618

# Tailoring cobalt spinel oxide with site-specific single atom incorporation for high-performance electrocatalysis†

Kangjae Lee,‡[ab] Jaehyuk Shim,‡[ab] Hyunsoo Ji,‡[ab] Jungho Kim,[f] Hyeon Seok Lee,[ab] Heejong Shin,[ab] Megalamane S. Bootharaju,[ab] Kug-Seung Lee,[c] Wonjae Ko,[ab] Jaewoo Lee,[ab] Kang Kim,[ab] Seungwoo Yoo,[ab] Sungeun Heo,[ab] Jaeyune Ryu,[ab] Seoin Back,*[f] Byoung-Hoon Lee,*[de] Yung-Eun Sung*[ab] and Taeghwan Hyeon*[ab]

Received 5th January 2024,
Accepted 15th April 2024

DOI: 10.1039/d4ee00058g

rsc.li/ees

Universal incorporation of metals into cobalt spinel oxide (CSO) has emerged as a versatile and promising strategy to enhance catalytic performance. However, the uncontrolled reactivity of early transition metal and metalloid precursors with water has presented a significant challenge in achieving atomic-scale metal incorporation within CSO. This study presents a groundbreaking approach for the atomic-scale integration of diverse dopants, including Hf, Ta, W, Ti, Pd, Ga, and Ge, while elucidating the atomic stabilization sites for these metal cations within CSO. Notably, certain metals, such as Ta, W, and Ge exhibit greater stability at the surface rather than within the core of CSO, resulting in a $Co^{2+}$-enriched surface that serves as a both catalytically active and protective shell. Exploiting these remarkable features, Ta-doped $Co_3O_4$ demonstrates the lowest overpotential, registering a mere 378 mV at 10 mA $cm^{-2}$, while maintaining its catalytic activity for over 140 hours in acidic electrolyte.

## Broader context

Spinel oxides with $AB_2O_4$ crystal structure have attracted significant attention due to their versatility in accommodating various metal compositions and the corresponding range of physicochemical properties. Cobalt spinel oxide, for instance, shows promise as a cost-effective catalyst for oxygen evolution reaction (OER). However, incorporation of metal elements into cobalt spinel oxide has been predominantly limited to first-row transition metal elements. Herein, we incorporate a wide range of elements into cobalt spinel oxide from early-transition metals to metalloids (including Hf, Ta, W, Ti, Ga, Ge, and Pd), which offers new possibilities. In addition, our research pinpoints specific stabilization sites for these metal elements within cobalt spinel oxide, with Ta, W, and Ge predominantly stabilized on the surface, resulting in a significant increase in surface $Co^{2+}$ species. This dopant-enriched shell serves both as an active layer and a protective layer, enhancing the performance of acidic OER. Leveraging these remarkable features, Ta-doped $Co_3O_4$ demonstrates the lowest overpotential, registering a mere 378 mV at 10 mA $cm^{-2}$, while maintaining its catalytic activity for over 140 hours in acidic electrolytes.

## Introduction

The performance of heterogeneous catalysts critically depends on surface characteristics,[1–3] underscoring the imperative need for meticulous control over electronic structure and chemical composition.[4–6] In this context, spinel oxides, featuring the $AB_2O_4$ crystal structure, have attracted significant attention as catalysts owing to their tunable physicochemical properties enabled by precise control over the composition of cationic A and B sites.[7–12] In particular, incorporation of various metal cations into cobalt spinel oxide (CSO, $Co_3O_4$) has emerged as a potent approach for precisely tailoring the catalytic properties of CSOs, in the context of a wide range of electrocatalytic reactions.[13–16]

---

[a] *Center for Nanoparticle Research, Institute for Basic Science (IBS), Seoul 08826, Republic of Korea*
[b] *School of Chemical and Biological Engineering, and Institute of Chemical Processes, Seoul National University, Seoul 08826, Republic of Korea*
[c] *Pohang Accelerator Laboratory (PAL), Pohang University of Science and Technology (POSTECH), Pohang, Republic of Korea*
[d] *KU-KIST Graduate School of Converging Science and Technology, Korea University, Seoul 02481, Republic of Korea*
[e] *Department of Integrative Energy Engineering, College of Engineering, Korea University, Seoul 02481, Republic of Korea*
[f] *Department of Chemical and Biomolecular Engineering, Institute of Emergent Materials, Sogang University, Seoul 04107, Republic of Korea*

† Electronic supplementary information (ESI) available. See DOI: **https://doi.org/10.1039/d4ee00058g**

‡ These authors contributed equally to this work.

Designing catalytic systems for the oxygen evolution reaction (OER) in acidic conditions is a subject of great interest.[17–21] The primary challenge in advancing acidic OER lies in the slow kinetics and the reliance on precious metals like Ru and Ir.[22–25] Notably, the CSO system has showcased substantial potential as a non-noble metal catalyst for acidic OER, offering a promising alternative to scarce and expensive noble metals.[26–28] A key strategy to address these challenges involves the deliberate incorporation of metal cations into a specific cobalt oxide platform.[29] Despite the suggested approach, current research has been predominantly limited to the integration of first-row transition metal ions, such as Fe, Mn, Ni, Cu, and Zn, which limits the range and scope of potential enhancements in the catalytic performance and durability of $Co_3O_4$.[30–34] Establishing a universal synthetic protocol enabling the incorporation of a diverse range of metal cations into the CSO system would usher in a new realm of possibilities for exploring novel catalytic materials.[35,36]

However, the process of identifying and effectively incorporating suitable cations for substitution in CSO remains elusive, primarily due to the limited understanding of the physicochemical characteristics governing the integration of a diverse range of metal cations into CSOs. Moreover, the inclusion of third-row early transition metals, such as Hf, Ta, and W, poses an even more intricate challenge, given their uncontrolled reaction with water, often leading to the undesired formation of heterogeneous oxides.[37,38] This chemical reaction obstructs the precise atomic-scale incorporation of these metals into $Co_3O_4$,[39,40] preventing the synthesis and catalytic applications of single atom catalysts based on third-row early transition metal doped in CSO.[41]

In this work, we provide a comprehensive understanding of the incorporation of metal cations into CSO. First, we have developed a versatile synthetic method that enables synthesizing various metal-doped CSO materials, including metal cations from early transition metals and metalloids. The metal organic framework (MOF) played a pivotal role in the successful synthesis of Hf, Ta, W, Ti, Pd, Ga, and Ge-incorporated CSO without the unwanted formation of hetero-metal-oxide species. Secondly, we have elucidated that each metal species occupies distinct stabilization sites within the cobalt spinel structure. Ta, W, and Ge tend to stabilize at the octahedral sites on the surface of CSO, significantly increasing the surface $Co^{2+}$ species. This dopant-rich shell and the high density of surface $Co^{2+}$ provide active and protective layers, resulting in high-performance in acidic OER. For instance, Ta-doped $Co_3O_4$ exhibited the lowest overpotential of 378 mV at 10 mA $cm^{-2}$, and maintained its activity for over 140 hours in acidic electrolytes. Our *in situ* X-ray absorption spectroscopy (XAS) and inductively coupled plasma (ICP) analysis indicate that this protective shell effectively suppresses over-oxidation and the dissolution of Co species during the reaction.

## Results and discussion

### Catalyst design and characterization

To synthesize metal-doped CSO, ZIF-67 MOF was selected as the source of cobalt. The dopant precursor is metal ethoxide, which is stabilized in methanol to mitigate the formation of hetero-metal-oxides. The dopant precursor was introduced during the rapid formation of ZIF-67 at room temperature, effectively confining the metal ethoxide within the pores of ZIF-67. Our encapsulation approach proved highly successful in preventing the generation of hetero-metal oxide byproducts, even after drying the as-synthesized material (Fig. S1, ESI†). Furthermore, this encapsulation method preserves the precursor in its single-atom-state, and the subsequent oxidation in a muffle furnace causes the MOF structure to rapidly disintegrate (Fig. S2, ESI†), resulting in the production of single-atom-doped CSO (Fig. 1a).[42]

Powder X-ray diffraction (XRD) analysis revealed the presence of peaks corresponding exclusively to CSO crystal planes, indicating that no secondary heterogeneous metal phases were formed during the oxidation process (Fig. S3, ESI†). Atomic-resolution high-angle annular dark-field scanning transmission electron microscopy (HAADF-STEM) clearly showed the atomic-scale incorporation of metal dopants throughout the CSO (Fig. 1b–d). In conjunction with the STEM images, we conducted XAS to gain deeper insights into the local atomic structure of single-atom dopants. According to the X-ray absorption near edge spectroscopy (XANES) and X-ray photoelectron spectroscopy (XPS) data, the single-atom metal dopants possessed oxidation states similar to their metal oxide counterparts (Fig. 1e–g and Fig. S4, ESI†). However, the peak shape of the white line for the dopants differentiates from that of their respective metal oxide references. Specifically, upon the incorporation of metal dopants into the cobalt spinel structure, only peak broadening was observed for Hf, whereas peak splitting into two different peaks was observed for Ta and W in $L_3$-edge XAS spectra. The Hf, Ta, and W $L_3$-edge XAS spectra illustrate the transition of core electrons from the occupied 2p to the vacant 5d states of the respective metals. The observed peak splitting in the $L_3$-edge spectrum results from the increased energy gap between the $t_{2g}$ and $e_g$ states within the 5d orbitals. This phenomenon can be attributed to the robust octahedral hybridization of orbitals due to enhanced metal-oxygen coordination. These results reveal that the Hf, Ta, and W atoms are effectively stabilized in the octahedral sites of CSO.[43] This arrangement would foster enhanced orbital hybridization between the metal dopants and CSO, leading to the broadening of the 5d orbital energy gap. Furthermore, the extended X-ray absorption fine structure (EXAFS) analyses indicate the atomic dispersion of metal dopants, as the bond length between metal and oxygen slightly decreases upon the incorporation of dopants into the CSO structure (Fig. 1h–j).

In addition to early transition metals from the sixth row of the periodic table, including Hf, Ta, and W, we successfully incorporated Pd, Ga, Ge, and Ti dopants into the CSO using the same synthetic procedure. The characterization data, including STEM, energy-dispersive X-ray spectroscopy (EDS), and EXAFS, consistently confirm the atomic dispersion of single-atom dopants within the CSO (Fig. S5–S8, ESI†).

### Stabilization sites of single-atom dopants

To gain atomic-level fundamental insights into the effect of incorporated dopants on the physicochemical properties of

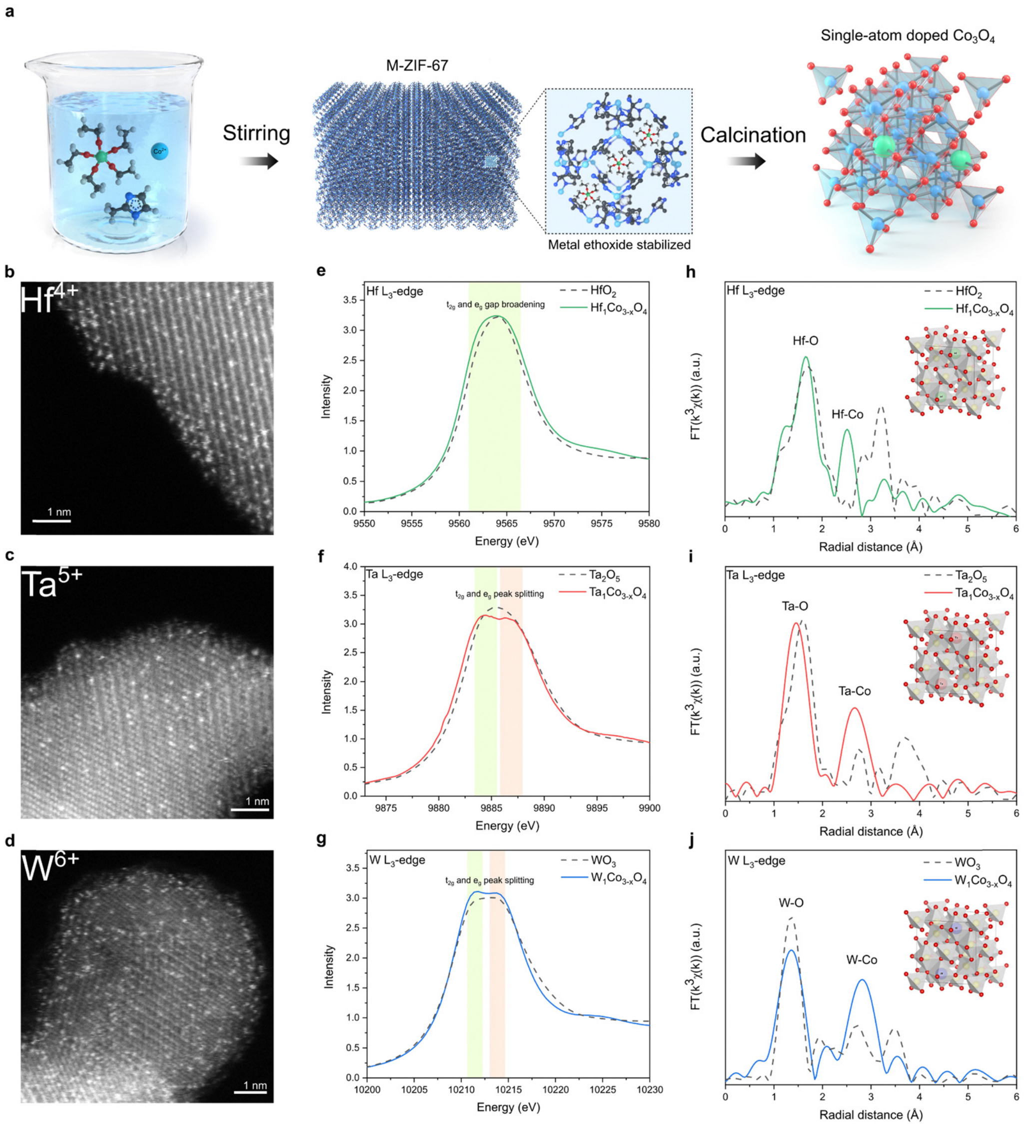

Fig. 1 Synthesis scheme and structural characterization. (a) Schematic illustration of synthetic process. HAADF-STEM images of (b) $Hf_1Co_{3-x}O_4$, (c) $Ta_1Co_{3-x}O_4$, (d) $W_1Co_{3-x}O_4$. The metal dopants were atomically incorporated in CSO crystal structure. $L_3$-edge XANES of (e) Hf in $Hf_1Co_{3-x}O_4$, (f) Ta in $Ta_1Co_{3-x}O_4$, and (g) W in $W_1Co_{3-x}O_4$. The d orbital broadening was observed. $L_3$-edge EXAFS of (h) Hf in $Hf_1Co_{3-x}O_4$, (i) Ta in $Ta_1Co_{3-x}O_4$, and (j) W in $W_1Co_{3-x}O_4$.

CSO, we conducted Co 2p XPS, Co L-edge XAS and Co K-edge XAS. XPS and Co L-edge XAS, known for their surface sensitivity, offer detailed information about the surface cobalt metal species.[44,45] The average oxidation state of Co changes (Fig. 2a) depending on the type of metal dopants, indicating that these dopants uniquely modify the electronic structure of CSO.[46,47] For a more comprehensive understanding, Co 2p XPS spectra were deconvoluted, displaying $Co^{3+}$ $2p_{3/2}$ peak at 779.2 eV and $Co^{2+}$ $2p_{3/2}$ peak at 780.6 eV (Table S1, ESI†). We calculated the ratio of $Co^{2+}$ to $Co^{3+}$, which is an indicator of the oxidation state of surface cobalt after the incorporation of metal cations. Notably, this ratio exhibited significant variations depending on the type of single-atom dopants, ranging from 0.959 (Pd) to 1.615 (Ge), displaying a maximum peak shift of 0.7 eV from the pristine CSO. To further elucidate the local coordination structure of the surface, we performed Co L-edge XAS. We observed that the spectra of all synthesized metal doped CSO's have the same shape with the pristine CSO, demonstrating the absence of change in the surface structure after the metal incorporation (Fig. S9, ESI†).

Unlike XPS, which offers surface-specific information, the Co K-edge XAS data provide insights into the bulk properties. As shown in Fig. 2b, all the metal-doped CSOs exhibit a uniform XANES structure and oxidation state, indicating that the Co oxidation state within the bulk oxide remains nearly unchanged. Moreover, the Co K-edge EXAFS, as shown in Fig. 2c, revealed no discernible differences in the local structure of the bulk CSO. Therefore, in contrast to the cobalt species on the surface, it appears that the bulk cobalt species remain unaffected by the incorporation of various types of metal ions.

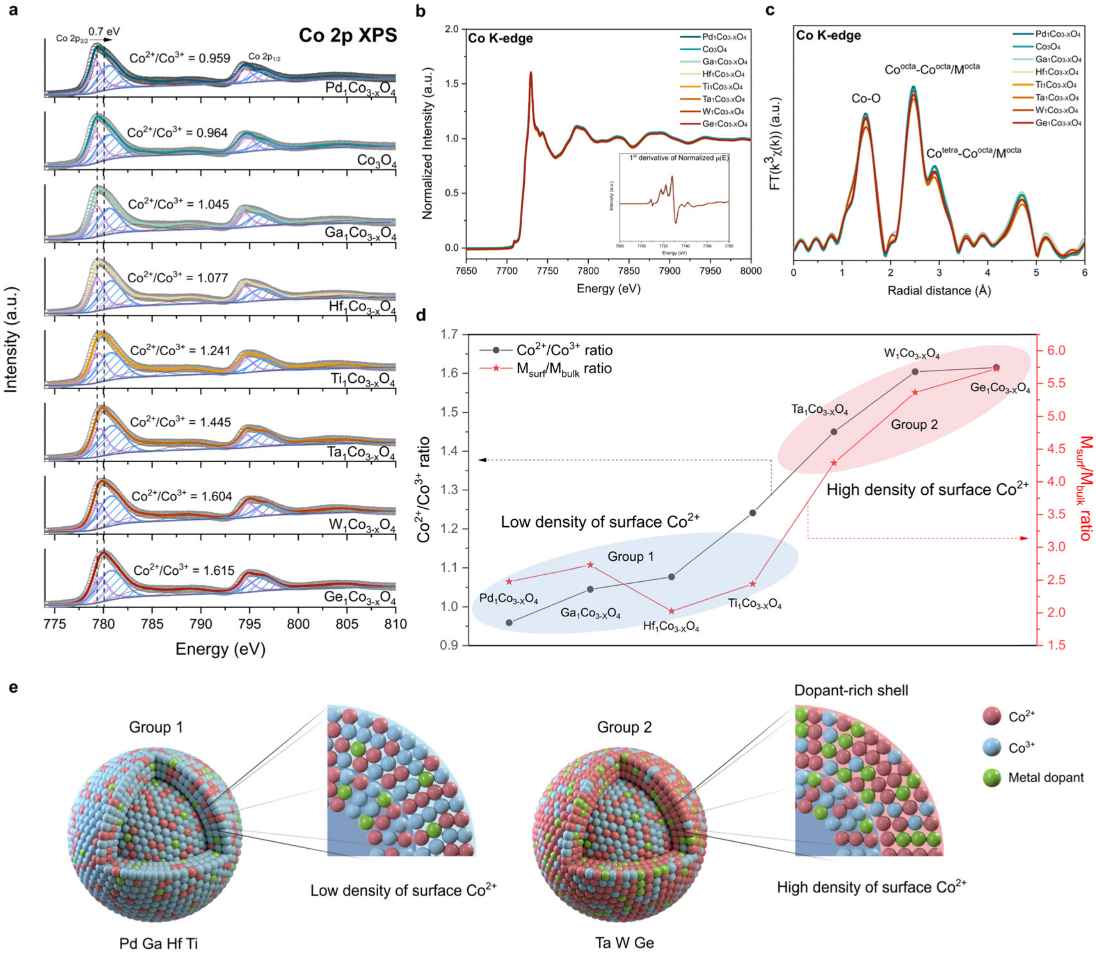

Fig. 2 Electronic structure of metal-doped $Co_3O_4$. (a) Co 2p XPS, (b) Co K-edge XANES, and (c) Co K-edge EXAFS spectra of metal-doped $Co_3O_4$. Inset of (b): 1st derivative of normalized $\mu(E)$. (d) $Co^{2+}/Co^{3+}$ ratio and $M_{surf}/M_{bulk}$ ratio of metal-doped $Co_3O_4$. The blue and red ellipses indicate group 1 and group 2 metals, respectively. (e) Schematic illustration of group 1 and group 2 metal-doped $Co_3O_4$. A dopant-rich shell is shown in the latter.

These combined data from XANES and XPS reveal that the dopants are primarily stabilized on the surface rather than within the bulk of CSO.

To characterize the specific sites of the stabilized metal dopants, we calculated the atomic ratio between metal dopants and cobalt on both the surface and the bulk of CSO. The atomic ratio of the surface ($M_{surf}$ = (atomic percent of metal dopants by XPS)/(atomic percent of Co by XPS)) was derived from the XPS results (Table S2, ESI†) and the atomic ratio of the bulk ($M_{bulk}$ = (atomic percent of metal dopants by ICP-AES)/(atomic percent of Co by ICP-AES)) was calculated based on the ICP-AES data (Table S3, ESI†). A high $M_{surf}/M_{bulk}$ ratio (group 2) implies that the metal dopants are predominantly stabilized on the surface of CSO, whereas a low $M_{surf}/M_{bulk}$ ratio (group 1) suggests that the metal dopants are evenly distributed throughout both the surface and bulk sites. Notably, Ta, W, and Ge exhibit high $M_{surf}/M_{bulk}$ ratios, exerting a considerable impact on the surface electronic structure and leading to a high density of surface $Co^{2+}$ species (Fig. 2d). On the other hand, Pd, Ga, Hf and Ti demonstrate low $M_{surf}/M_{bulk}$ ratios, which have minimal influence on the surface properties of CSO. We further calculated the stabilization energies of two slab structures: one with a dopant located in the first layer and the other with the dopant in the third layer. We assume that these positions correspond to the surface and the bulk position, respectively (Fig. S10 and S11, ESI†). The qualitative results are generally in agreement with the experimental observations, where Ta, Ge and W with large energy differences between two layers show a preference for surface positions, whereas Ga, Pd, Ti and Hf tend to prefer bulk positions.

From all these data, we conclude that the choice of metal dopants significantly impacts the surface characteristics of CSO, as illustrated in Fig. 2e. Notably, Ta, W, and Ge, categorized as group 2 metals, result in CSOs with dopant-rich shells that contain a high density of $Co^{2+}$ species on the surface. This result is corroborated by energy-filtered transmission electron microscopy (EF-TEM) and XPS depth profile. EF-TEM images demonstrate the uniform coverage of the surface with Ta single atoms (Fig. S12, ESI†). XPS depth profile shows that Ta is more stabilized on the near surface rather than in the bulk

(Fig. S13, ESI†). Because increased content of Ta species near the surface affects the peripheral Co electronic structure, Co species located closer to the surface tends to be more reduced, which is supported by Co 2p angle resolved-XPS (AR-XPS) spectra (Fig. S14, ESI†). Moreover, we analyzed the Bader charges of Co atoms before and after the Ta doping (Fig. S15, ESI†). The Bader charge values of Co atoms near the Ta dopant decrease by 0.15, which is consistent with Co 2p XPS. Additionally, scanning electron microscopy (SEM) analysis reveals that the dopant-rich shell serves as a protective layer,[45] preserving the dodecahedron morphology of ZIF-67 during calcination in the air (Fig. S16, ESI†).

### Catalytic performance

We next examined how the foregoing modifications of surface electronic structure and composition affect both catalytic activity and durability. To establish the correlation between these surface properties and catalytic performance, we evaluated the OER performance for all the synthesized catalysts using a rotating disk electrode (RDE) in a 0.05 M $H_2SO_4$ electrolyte. The recorded linear sweep voltammetry (LSV) curves for all the synthesized catalysts (Fig. 3a and b) reveal a noticeable enhancement in OER performance compared to bare $Co_3O_4$. By systematically varying the Ta content, we identified an optimal composition. The samples with varying amounts of Ta were designated as $Ta_1Co_{3-x}O_4$ (10 : 5) and $Ta_1Co_{3-x}O_4$ (10 : 1), representing higher and lower Ta content compared to $Ta_1Co_{3-x}O_4$, respectively (as detailed in Table S4, ESI†). In both cases, while the activity exhibited a decrease compared to $Ta_1Co_{3-x}O_4$, it remained superior to that of the bare $Co_3O_4$. We then investigated the OER catalytic activity of $Ta_1Co_{3-x}O_4$, where $Co_1$ is Co atom located right next to the Ta dopant, while $Co_2$ is the one far from the Ta single atom (Fig. S17, ESI†). The pristine $Co_3O_4$ is known to bind OER adsorbates weakly, making the *OH adsorption a rate-determining step (RDS) with the $\eta^{\mathrm{OER}}$ of 0.554 $V_{\mathrm{RHE}}$.[10] Once the Ta is doped, the binding affinity of OH* increased, changing the RDS to *O and *OOH formation for $Co_1$ and $Co_2$, respectively. $\eta^{\mathrm{OER}}$ decreased to 0.334 $V_{\mathrm{RHE}}$ for $Co_1$ and 0.489 $V_{\mathrm{RHE}}$ for $Co_2$. In contrast, the Ta single atom exhibited a high $\eta^{\mathrm{OER}}$ of 0.933 $V_{\mathrm{RHE}}$ with the *OOH formation step being the RDS. This indicates that incorporation of Ta within $Co_3O_4$ could enhance the OER activity, primarily by activating surface Co species. In Fig. 3c, we provide a summary of the overpotentials required to achieve a current density of 10 mA $cm^{-2}$ for all the measured samples. Notably, the most active $Ta_1Co_{3-x}O_4$ catalyst demonstrated an overpotential of 378 mV, 88 mV lower than that of $Co_3O_4$. Taken together, these studies demonstrate the significance of precise and controlled metal incorporation as a powerful tool for optimizing the OER performance of CSO systems (Table S5, ESI†).

We further investigated the durability trends across all the samples by comparing the increases in their overpotentials at a current density of 10 mA $cm^{-2}$ (Fig. 3d). The metals with the high $M_{\mathrm{surf}}/M_{\mathrm{bulk}}$ ratios (Ta, W, and Ge) showed a striking enhancement in acidic OER stability, suggesting that the dopant-rich shell could effectively function as a protective barrier in the face of harsh oxidative conditions. Among these,

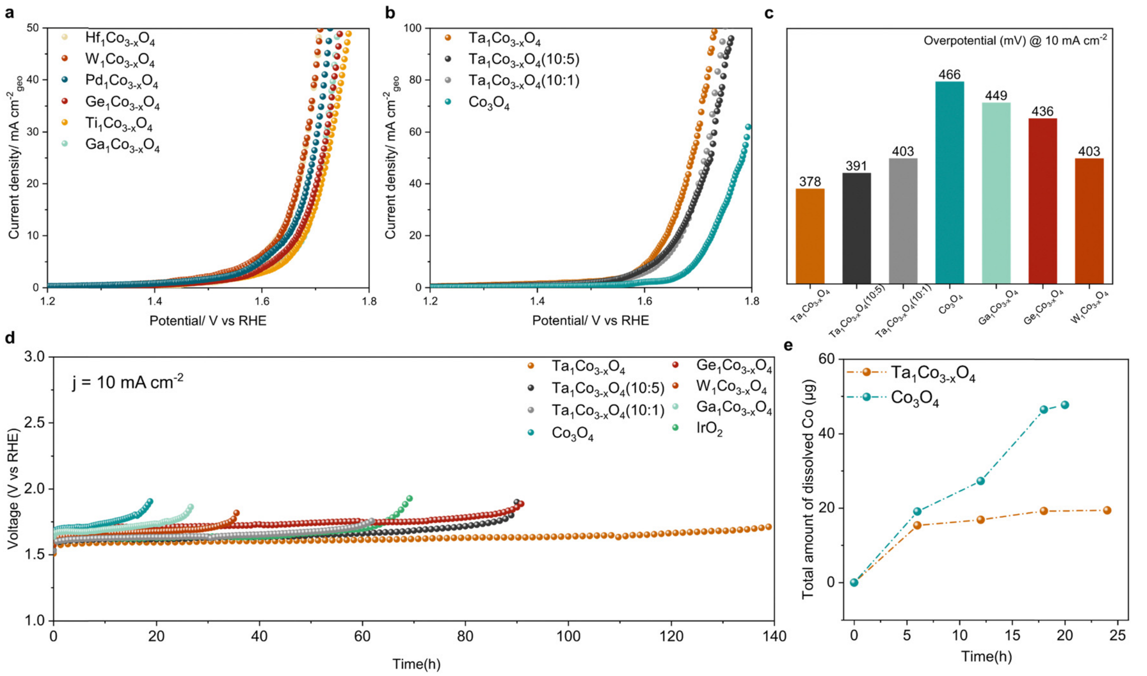

Fig. 3 Electrocatalytic acidic OER performance. (a) Linear sweep voltammetry (LSV) curves of $Co_3O_4$ doped with Hf, W, Pd, Ge, Ti, and Ga in 0.05 M $H_2SO_4$ electrolyte. (b) LSV curves of $Co_3O_4$ with varying Ta amounts. (c) Overpotential bar graph of catalysts in panels (a) and (b) at 10 mA $cm^{-2}$. (d) Chronopotentiometry curves of the synthesized catalysts and $IrO_2$ at 10 mA $cm^{-2}$. (e) Amount of dissolved cobalt ion measured by ICP-MS analysis during the stability test shown in panel (d).

$Ta_1Co_{3-x}O_4$ exhibited the most remarkable catalytic stability with no discernible decay in its activity observed over a 140-hour period, recording a degradation rate of 1.04 mV $h^{-1}$. In contrast, $Co_3O_4$ exhibited a rapid deterioration in activity after 19 hours, with a degradation rate of 11.67 mV $h^{-1}$, 11 times higher than that of $Ta_1Co_{3-x}O_4$. Additionally, we assessed the stability of $Ga_1Co_{3-x}O_4$ as a representative of metals belonging to the low $M_{surf}/M_{bulk}$ group (encompassing Ga, Hf, Ti, and Pd), which displayed minimal progress in terms of oxidative stability.

To further analyze the catalytic stability of $Ta_1Co_{3-x}O_4$ and $Co_3O_4$, we quantified the degree of cobalt ion dissolution following 24 hours of operation in an acidic OER environment (Fig. 3e).[48] The ICP results reveal that the introduction of Ta to the $Co_3O_4$ surface effectively mitigated the dissolution of cobalt species. Once the surface was stabilized during the reaction, $Ta_1Co_{3-x}O_4$ displayed a notably stabilized trend in dissolution, in stark contrast to the continuous dissolution observed in $Co_3O_4$. We calculated S-number based on the ICP results at 6-hour and 18-hour intervals (Fig. S18, ESI†). For $Ta_1Co_{3-x}O_4$, the S-number values were approximately $2.148 \times 10^3$ at the 6-hour mark and $5.138 \times 10^3$ at the 18-hour mark. In contrast, the S-number values for $Co_3O_4$ were approximately $1.730 \times 10^3$ at 6 hours and $2.130 \times 10^3$ at 18 hours. These values differed significantly, with $Ta_1Co_{3-x}O_4$ exhibiting a 1.24-fold at 6 hours and a 2.41-fold at 18 hours compared to $Co_3O_4$. This discrepancy shows the enhanced stability achieved through the incorporation of Ta on the surface, with the difference in stability becoming more pronounced as time progresses.

## Durability of catalyst

To demonstrate durability of the catalysts, we performed the post-OER characterization of $Ta_1Co_{3-x}O_4$. HAADF-STEM image and STEM-EDS mapping images of $Ta_1Co_{3-x}O_4$ reveal that atomically dispersed Ta metals maintained after OER. This result indicates that the Ta single atoms incorporated in CSO crystal structure remain stable during acidic OER (Fig. 4a and b). XRD patterns of $Ta_1Co_{3-x}O_4$ on carbon paper after OER showed the presence of peaks corresponding exclusively to CSO crystal planes, indicating no hetero-metal phase formed during the reaction (Fig. 4c).

Furthermore, an *in situ* XAS study was conducted on $Ta_1Co_{3-x}O_4$ to investigate changes in the electronic structure during electrochemical reaction (Fig. 4d). Remarkably, *in situ* XANES spectra of $Ta_1Co_{3-x}O_4$ showed negligible alteration in oxidation state as the applied voltage increased in acidic electrolytes, demonstrating the dopant-rich shell and high density of surface $Co^{2+}$ suppresses the overoxidation of Co species during OER.

Additionally, *ex situ* investigations of XPS were carried out on post-OER samples (Fig. 4e).[49] The distinct $Co^{2+}$ XPS peaks of $Ta_1Co_{3-x}O_4$ were observed after OER, indicating that the $Co^{2+}$

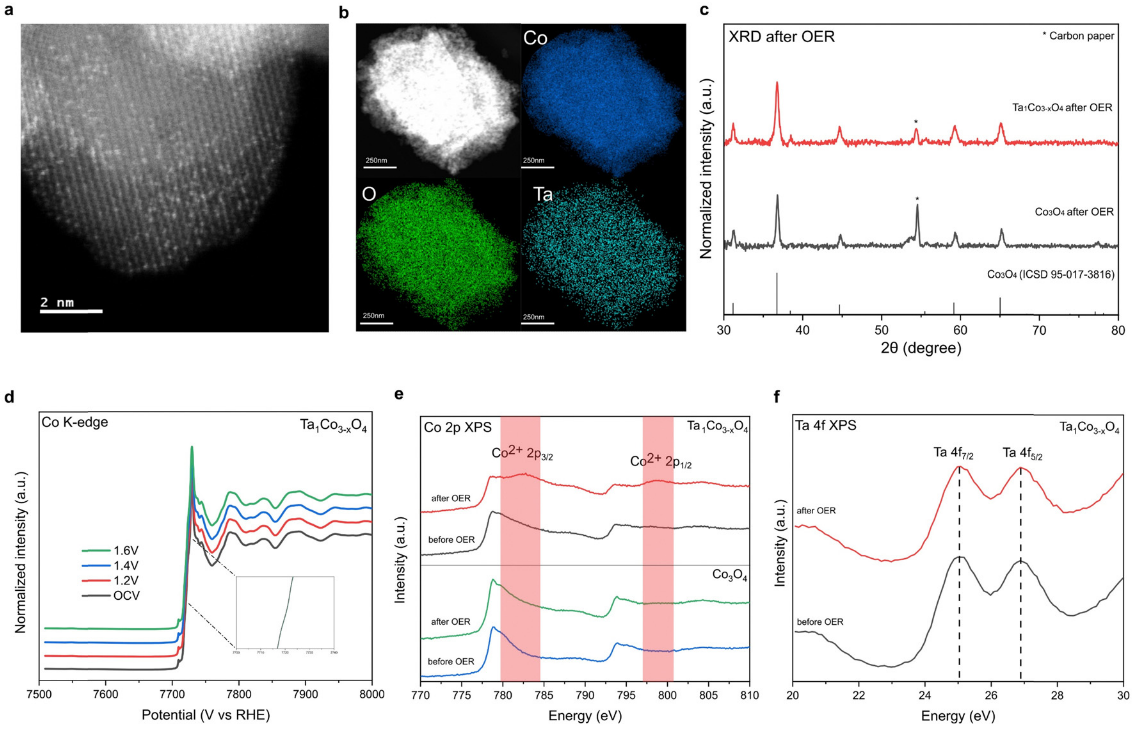

Fig. 4 Post-OER characterization of $Ta_1Co_{3-x}O_4$. (a) HAADF-STEM image of $Ta_1Co_{3-x}O_4$ after OER. (b) STEM-EDS mapping images of $Ta_1Co_{3-x}O_4$ after OER. The atomically dispersed Ta atoms maintained without aggregation after OER. (c) XRD patterns of $Ta_1Co_{3-x}O_4$ on carbon paper after OER. The patterns indicated that $Co_3O_4$ structure maintained after OER. (d) *In situ* XANES spectra of $Ta_1Co_{3-x}O_4$ at different applied potentials in 0.05 M $H_2SO_4$. (e) Co 2p XPS spectra of $Ta_1Co_{3-x}O_4$ and $Co_3O_4$ before and after the OER stability test. The surface $Co^{2+}$ remained even after long-term acidic OER. (f) Ta 4f XPS of $Ta_1Co_{3-x}O_4$ after OER showed that the oxidation state of surface Ta maintained after OER.

species in the form of Ta–O–Co are significantly more stable compared to $Co^{3+}$ species in oxidative condition. The stability of the Ta single atom, as evidenced by the HAADF-STEM image, along with the absence of hetero-phase formation, supports the conclusion that the Co metal species in close proximity to the Ta single atom remain stable during OER. During the course of the reaction, the less stable surface $Co^{3+}$ species dissolve, leaving behind $Co^{2+}$ species alongside Ta dopants, which play a pivotal role in enhancing the durability of $Ta_1Co_{3-x}O_4$ in acidic electrolytes. Conversely, the Co 2p XPS spectra of $Co_3O_4$ control exhibit minimal changes after OER, which can be attributed to the ongoing dissolution of surface Co species during the OER process. This observation is consistent with the findings from the aforementioned 24-hour *ex situ* ICP analysis, which revealed a persistent dissolution of Co ions in the $Co_3O_4$ control, while no further dissolution of Co was observed in $Ta_1Co_{3-x}O_4$ after the initial 5 hours (Fig. 3e). Ta 4f XPS of $Ta_1Co_{3-x}O_4$ showed that the oxidation state of Ta maintained after OER (Fig. 4f). We also calculated dissolution potentials ($U_{\mathrm{diss}}$) of tetrahedral $Co^{2+}$ atoms in both pure $Co_3O_4$ and $Ta_1Co_{3-x}O_4$ to evaluate the stability of $Co^{2+}$ species after the incorporation of Ta (Fig. S19, ESI†). A higher $U_{\mathrm{diss}}$ indicates higher stability against the dissolution during acidic OER. We found that the $U_{\mathrm{diss}}$ of tetrahedral $Co^{2+}$ increased from 1.25 $V_{\mathrm{SHE}}$ to 1.58 $V_{\mathrm{SHE}}$ upon doping with Ta, signifying that Ta dopants effectively prevent the dissolution of tetrahedral $Co^{2+}$. Collectively, the dopant-rich shell serves to preserve the presence of surface $Co^{2+}$ species throughout the reaction, effectively inhibiting the dissolution of surface Co species.

To investigate the possibility of a newly constructed surface structure contributing to enhanced OER performance as $Co^{3+}$ species dissolve, we conducted CS-TEM analysis on the catalyst surface after OER. It turned out that lattice near the surface maintained the initial CSO structure without forming new amorphous or crystalline surface structures (Fig. S20, ESI†). Moreover, the Co L-edge XAS spectra of post-OER catalysts consistently show an absence of alteration in the surface structure after acidic OER (Fig. S21, ESI†).

# Conclusion

In summary, we present a comprehensive understanding of the crystal structure of single-atom-doped CSO and introduce a general synthetic method applicable to a wide spectrum of metal elements, extending beyond the first-row transition metals. The encapsulation method effectively stabilizes water-sensitive metal precursors, including early-transition metal and metalloid, thus enabling the precise incorporation of diverse metal elements at the atomic scale within CSO. Our experimental results demonstrate the successful atomic distribution of metal dopants in CSO, with no discernible formation of hetero-metal-oxide species. Furthermore, we unveiled the metal-specific stabilization sites in CSO, revealing distinctive surface physicochemical properties for each metal. These finely controlled surface properties have the potential to translate into improved catalytic performance and enduring stability during acidic OER. Our discovery in the general synthesis of incorporating multiple metals into CSO and controlling resulting surface properties has promising applications across a broad spectrum of catalytic processes in sustainable energy storage and conversion systems.

# Experimental methods

## Materials and methods

**Materials.** Cobalt(II) nitrate hexahydrate ($Co(NO_3)_2{\cdot}6H_2O$, ≥99.9%), 2-methylimidazole (99%), tantalum(V) ethoxide ($Ta(CH_3CH_2O)_5$, 99.98%), germanium(IV) ethoxide ($Ge(CH_3CH_2O)_4$, ≥99.95%), titanium(IV) ethoxide ($Ti(CH_3CH_2O)_4$, technical grade), palladium(II) acetylacetonate ($Pd(acac)_2$, 99%) and sulfuric acid (98%) were purchased from Sigma-Aldrich. Gallium(III) ethoxide ($Ga(CH_3CH_2O)_3$), hafnium(IV) ethoxide ($Hf(CH_3CH_2O)_4$, 99.9%), and tungsten(V) ethoxide ($W(CH_3CH_2O)_5$) were purchased from Thermo Fisher Scientific. Methyl alcohol (MeOH, 99.8%) was purchased from Samchun Chemical. To utilize as a reference group for X-ray photoelectron spectroscopy (XPS) and X-ray absorption spectroscopy (XAS), commercial metal oxide was purchased. Cobalt(II,III) oxide ($Co_3O_4$, 99.5%), titanium(IV) oxide ($TiO_2$, ≥99%), gallium(III) oxide ($Ga_2O_3$, ≥99.99%), germanium(IV) oxide ($GeO_2$, ≥99.99%), hafnium(IV) oxide ($HfO_2$, 98%), tantalum(V) oxide ($Ta_2O_5$, 99%), tungsten(VI) oxide ($WO_3$, 99.9%), and palladium(II) oxide (PdO, 99.97%) were all purchased from Sigma-Aldrich. Ultrapure deionized (DI) water (Milli-Q grade, 18.2 Ωm resistivity, TOC level < 2 ppb) was obtained from a Milli-Q water purification system.

**Methods**

*Synthesis of ZIF-67.* Synthetic method was slightly modified to improve its extensibility of various elements incorporation.[27] To synthesize ZIF-67, 40 mL of MeOH (solution A) solution which fully dissolved 1313.6 mg of 2-methylimidazole was prepared. Another 40 mL of MeOH which dissolved 580.1 mg of $Co(NO_3)_2{\cdot}6H_2O$ was prepared and directly added to solution A with vigorous stirring at room temperature. After 18 hours, ZIF-67 precipitate was obtained by centrifugation, which was followed by washing with MeOH. The precipitate was dried for several hours under vacuum (60 °C).

*Synthesis of $Co_3O_4$.* As-synthesized violet powders were heated at 400 °C for 4 h under air in a muffle furnace with a ramping rate of 5 °C $min^{-1}$. After cooling, black powder was acquired.

*Synthesis of $Ta_1Co_{3-x}O_4$.* $Ta_1Co_{3-x}O_4$ was synthesized using the same procedure employed for the synthesis of $Co_3O_4$, except that $Ta(CH_3CH_2O)_5$ was used during the synthesis of ZIF-67. 0.6 mmol of $Ta(CH_3CH_2O)_5$ was well dispersed in MeOH solution. Maintaining the total volume of the solution at 80 mL, all solutions were mixed together with vigorous stirring to obtain violet solution.

*Synthesis of $Ta_1Co_{3-x}O_4$ (10 : 1).* $Ta_1Co_{3-x}O_4$ (10 : 1) was synthesized using the same procedure employed for the synthesis of $Co_3O_4$, except that $Ta(CH_3CH_2O)_5$ was used during the synthesis of ZIF-67. 0.2 mmol of $Ta(CH_3CH_2O)_5$ was well dispersed in MeOH solution. Maintaining the total volume of the solution at 80 mL, all solutions were mixed together with vigorous stirring to obtain violet solution.

*Synthesis of $Ta_1Co_{3-x}O_4$ (10 : 5).* $Ta_1Co_{3-x}O_4$ (10 : 5) was synthesized using the same procedure employed for the synthesis of $Co_3O_4$, except that $Ta(CH_3CH_2O)_5$ was used during the synthesis of ZIF-67. 1 mmol of $Ta(CH_3CH_2O)_5$ was well dispersed in MeOH solution. Maintaining the total volume of the solution at 80 mL, all solutions were mixed together with vigorous stirring to obtain violet solution.

*Synthesis of $Hf_1Co_{3-x}O_4$.* $Hf_1Co_{3-x}O_4$ was synthesized using the same procedure employed for the synthesis of $Co_3O_4$, except that $Hf(CH_3CH_2O)_4$ was used during the synthesis of ZIF-67. 0.2 mmol of $Hf(CH_3CH_2O)_4$ was well dispersed in MeOH solution. Maintaining the total volume of the solution at 80 mL, all solutions were mixed together with vigorous stirring to obtain violet solution.

*Synthesis of $W_1Co_{3-x}O_4$.* $W_1Co_{3-x}O_4$ was synthesized using the same procedure employed for the synthesis of $Co_3O_4$, except that $W(CH_3CH_2O)_6$ was used during the synthesis of ZIF-67. 0.2 mmol of $W(CH_3CH_2O)_6$ was well dispersed in MeOH solution. Maintaining the total volume of the solution at 80 mL, all solutions were mixed together with vigorous stirring to obtain violet solution.

*Synthesis of $Ti_1Co_{3-x}O_4$.* $Ti_1Co_{3-x}O_4$ was synthesized using the same procedure employed for the synthesis of $Co_3O_4$, except that $Ti(CH_3CH_2O)_4$ was used during the synthesis of ZIF-67. 0.2 mmol of $Ti(CH_3CH_2O)_4$ was well dispersed in MeOH solution. Maintaining the total volume of the solution at 80 mL, all solutions were mixed together with vigorous stirring to obtain violet solution.

*Synthesis of $Ga_1Co_{3-x}O_4$.* $Ga_1Co_{3-x}O_4$ was synthesized using the same procedure employed for the synthesis of $Co_3O_4$, except that $Ga(CH_3CH_2O)_3$ was used during the synthesis of ZIF-67. 0.6 mmol of $Ga(CH_3CH_2O)_3$ was well dispersed in MeOH solution. Maintaining the total volume of the solution at 80 mL, all solutions were mixed together with vigorous stirring to obtain violet solution.

*Synthesis of $Ge_1Co_{3-x}O_4$.* $Ge_1Co_{3-x}O_4$ was synthesized using the same procedure employed for the synthesis of $Co_3O_4$, except that $Ge(CH_3CH_2O)_4$ was used during the synthesis of ZIF-67. 0.6 mmol of $Ge(CH_3CH_2O)_4$ was well dispersed in MeOH solution. Maintaining the total volume of the solution at 80 mL, all solutions were mixed together with vigorous stirring to obtain violet solution.

*Synthesis of $Pd_1Co_{3-x}O_4$.* $Pd_1Co_{3-x}O_4$ was synthesized using the same procedure employed for the synthesis of $Co_3O_4$, except that $Pd(acac)_2$ was used during the synthesis of ZIF-67. 0.2 mmol of $Pd(acac)_2$ was well dispersed in MeOH solution. Maintaining the total volume of the solution at 80 mL, all solutions were mixed together with vigorous stirring to obtain violet solution.

### Characterization

Atomic-resolution high-angle annular dark-field scanning transmission electron microscopy (HAADF-STEM) was conducted at 200 kV with a spherical aberration-corrected JEM ARM-200F (Cold FEG Type, JEOL) installed at the National Center for Inter-University Research Facilities at Seoul National University. CS-TEM was conducted at 200 kV with a spherical aberration-corrected JEM ARM200F (Cold FEG Type, JEOL) equipped with OneView camera (25 fps at full 4k × 4k resolution) and Orius SC200D camera (2k × 2k resolution) at the National Center for Inter-University Research Facilities at Seoul National University. XANES and EXAFS spectra were acquired using beamline 8C nano XAFS and 10C wide XAFS installed at Pohang light source II in Pohang accelerator laboratory. All XAS measurements were carried out with the transmission mode. Calibration of $E_0$ values of each sample was performed based on the simultaneously measured $E_0$ value of each metal reference foils. *In situ* XAFS data at the Co K-edge were acquired at the 8c beamline of the Pohang Accelerator Laboratory in Korea, employing the fluorescence mode, while the measurements were conducted within an electrolysis cell. Software ATHENA was used to reduce data to get XANES and EXAFS spectra. XPS measurements were performed by K-Alpha+ XPS system (Thermo Fisher Scientific) using X-ray source as microfocused monochromated Al-Kα (1486.6 eV) at the Korea Basic Science Institute in Busan. XPS was conducted with high resolution of step size 0.1 eV in the energy range where the peaks were located. All spectra were calibrated by C 1s binding energy of graphite. XPS depth profile and AR-XPS were conducted by K-alpha (Thermo Scientific Inc., U.K.) using X-ray source (12 kV, 3 mA) as monochromated Al-Kα (1486.6 eV) at the Yonsei cooperative center for research facilities. Argon etching (500 eV) was employed to etch the surface of the pellet and XPS was measured every 30 s. AR-XPS was conducted with a high resolution of a step size 0.1 eV. All spectra were calibrated using the C 1s binding energy. Powder XRD patterns were collected using a SmartLab (Rigaku) diffractometer with Cu Kα radiation. EDS mapping and corresponding STEM images were obtained using STEM mode equipped with a single drift detector (X-MAX$^N$, Oxford Instruments). Energy filtered transmission electron microscopy (EF-TEM) images were obtained using GIF mode of TEM (JEM ARM-200F) equipped with 965 GIF Quantum ER. SEM images were collected using SIGMA (Carl Zeiss). To prepare SEM samples, platinum was sputtered on the samples using sputter coater EM ACE200 (Leica). The bulk composition of Co and other metal elements was collected using ICP-AES (OPTIMA 8300) except that Ge and W which are hardly decomposed so that they need to be dissolved in hydrofluoric acid. Their composition was measured using Agilent 5110, treated with hydrofluoric acid. Dissolved cobalt ions during the reaction were subjected to small fractional extraction at specified intervals, followed by subsequent ICP-MS analysis (Varian 820-MS). Thermogravimetric analysis (TGA) was conducted by an SDT-Q600 (TA instruments) ramping to 600 °C with ramping rate 10 °C $\text{min}^{-1}$ and air purging (100 mL $\text{min}^{-1}$). IR spectroscopy was performed using VERTEX 70v (Bruker) at room temperature under vacuum. IR spectra was obtained averaging 300 scans per spectra at a spectral resolution of 0.5 $\text{cm}^{-1}$ after background measurement.

### Electrochemical analysis

Electrochemical measurements were conducted under controlled conditions in a 0.05 M $H_2SO_4$ electrolyte solution (pH = 1.0) at 25 °C. A three-electrode system was employed, utilizing an Autolab potentiostat (PGSTAT302N) for data acquisition. The working electrode consisted of a rotating disk electrode (RDE) paired with a glassy carbon electrode (surface area of 0.1965 $\text{cm}^2$). An Ag/AgCl electrode served as the reference electrode, while a platinum sheet functioned as the counter electrode. All potentials were recalibrated using the following formula: $E_{\text{RHE}} = E_{\text{Ag/AgCl}} + 0.1976 + 0.0591 \times \text{pH} = E_{\text{Ag/AgCl}} + 0.2567$. In the preparation of the catalyst ink on the glassy carbon electrode, a mixture of 5 mg of the catalyst and 1.67 mg of Vulcan Carbon was dispersed in a 1 mL solution composed of 970 μl of deionized (DI) water and isopropanol in a volume ratio of 2 : 8, along with 30 μl of a 5% Nafion solution. Subsequently, the resulting mixtures underwent ultrasonication for approximately 1 hour to achieve uniform ink dispersion. Using a spin-coating technique, 17.64 μl of the dispersed ink was deposited onto a glassy carbon electrode, resulting in a catalyst loading of 0.45 mg $\text{cm}^{-2}$. Subsequently, linear sweep voltammetry (LSV) with an 100% iR correction was conducted at an ambient temperature of 25 °C, employing a scan rate of 0.01 V $\text{s}^{-1}$ and a working electrode rotating at 1600 rpm. For stability assessments on carbon papers, 5 mg of the catalyst was dispersed in a 1 mL solution consisting of 970 μl isopropanol and deionized (DI) water in a volume ratio of 8 : 2, complemented by the addition of 30 μl of a 5% Nafion solution. Following approximately 1 hour of ultrasonication, the resulting ink was evenly deposited onto a carbon paper substrate *via* air spraying, achieving a loading of 3 mg $\text{cm}^{-2}$. To ensure accurate mass loading, the carbon paper's weight was measured both before and after the air spraying process. In the case of the commercial $IrO_2$ catalyst, the loading was adjusted to 1 mg $\text{cm}^{-2}$.

The S-number values were calculated from the catalyst on a carbon paper during the stability test. The S-number was calculated according to eqn (1),

$$\text{S-number} = \frac{n_{O_2}}{n_{\text{cobalt metal}}}.$$

$n_{O_2}$ represents the cumulative quantity of evolved oxygen determined from the total charge obtained during the chronopotentiometry test, while "$n_{\text{cobalt metal}}$" refers to the amounts of leached Co determined from the results of ICP-MS.

### Computational detail

Spin-polarized density functional theory (DFT) calculations were performed using the Vienna ab initio simulation package (VASP) version 5.4.4.[50,51] The Perdew–Burke–Ernzerhof (PBE) exchange–correlation functional and the projector augmented wave (PAW) pseudopotential were employed.[52–54] A Hubbard $U$ correction method was applied with the effective $U_{\text{eff}}$ ($U - J$) value of 3.32 eV for Co to take into account strong on-site Coulombic interactions of localized d-orbitals.[55] The optimized magnetic moments of the octahedral and tetrahedral Co atoms were 0.00 and 2.75, which correspond to low-spin $\text{Co}^{3+}$ and high-spin $\text{Co}^{2+}$, respectively.[9] The metallic bulk Co structure (mp-102) was calculated without this $U$ correction. A kinetic energy cutoff of 500 eV was set for all calculations. Convergence for forces and energies was considered reached when they become smaller than $10^{-4}$ eV and 0.05 eV $\text{Å}^{-1}$ for slab structures and $10^{-5}$ eV and 0.01 eV $\text{Å}^{-1}$ for bulk structures, respectively. Monkhorst–Pack *k*-points were set at 3 × 3 × 1 for slab structures and 4 × 4 × 4 for bulk structures.[56]

A four-layered cobalt spinel (001) slab structure was modelled using the corresponding optimized bulk structure (mp-18748). A vacuum space of 15 Å was added in the $z$-direction and the bottom two layers were fixed to their bulk positions. Starting with this optimized slab structures, transition metal doped structures were created by substituting the octahedral Co in the first and the third layer with dopant atoms. We note that the positions of the dopant in the first and third layers represent the surface and bulk positions, respectively. To calculate the dissolution potentials, defective structures were generated by removing octahedral or tetrahedral Co atoms from the first layer.

The theoretical overpotential for OER was calculated using the computational hydrogen electrode (CHE) method.[57] This method equates the chemical potentials of the proton-electron pair ($H^+ + e^-$) with half of $H_2$ gas under standard conditions. Following the adsorbate evolution mechanism (AEM),[58] which involves four consecutive proton–electron transfers ($* + H_2O \rightarrow {}^*OOH \rightarrow {}^*O + H_2O \rightarrow {}^*OH \rightarrow * + O_2$), the Gibbs free energy change for each step was calculated as follows:

$$\Delta G_1 = G_{\text{OH}*} - G_* - G_{\text{H}_2\text{O}} + 0.5G_{\text{H}_2} \tag{1}$$

$$\Delta G_2 = G_{\text{O}*} - G_{\text{OH}*} + 0.5G_{\text{H}_2} \tag{2}$$

$$\Delta G_3 = G_{\text{OOH}*} - G_{\text{O}*} - G_{\text{H}_2\text{O}} + 0.5G_{\text{H}_2} \tag{3}$$

$$\Delta G_4 = G_* - G_{\text{OOH}*} + 0.5G_{\text{H}_2} + 4.92\ \text{eV} \tag{4}$$

where $G_*$, $G_{\text{O}*}$, $G_{\text{OH}*}$, $G_{\text{OOH}*}$, $G_{\text{H}_2}$, $G_{\text{H}_2\text{O}}$ are the Gibbs free energies of bare surface, O, OH, OOH-adsorbed surfaces, $H_2$ and $H_2O$ gas, respectively. The Gibbs free energies were calculated by adding free energy correction values to DFT energies, where the correction term consists of zero-point energies, enthalpic and entropic contributions. These correction values were calculated using the Harmonic oscillator and the Ideal gas approximation for adsorbates and gas molecules, respectively, as implemented in atomic simulation environment (ASE).[59] The theoretical overpotential was determined as the difference between the equilibrium potential of 1.23 V and the largest Gibbs free energy change, *i.e.*, $\eta^{\text{OER}} = \max(\Delta G_1,\Delta G_2,\Delta G_3,\Delta G_4)/e - 1.23$ V.

The electrochemical stability of Co against the dissolution was investigated considering the following reaction:

$$\mathrm{Co}_{x-1}\mathrm{O}_y + \mathrm{Co}^{z+} + ze^- \rightleftharpoons \mathrm{Co}_x\mathrm{O}_y \qquad (5)$$

and the Gibbs free energy change of the dissolution of Co ($\Delta G_{\mathrm{diss}}$) was calculated as

$$\Delta G_{\mathrm{diss}} = E_{\mathrm{Co}_x\mathrm{O}_y} - E_{\mathrm{Co}_{x-1}\mathrm{O}_y} - E_{\mathrm{Co}^{z+}+ze^-} \qquad (6)$$

$$= (E_{\mathrm{Co}_x\mathrm{O}_y} - E_{\mathrm{Co}_{x-1}\mathrm{O}_y} - E_{\mathrm{Co}}) + (E_{\mathrm{Co}} - E_{\mathrm{Co}^{z+}+ze^-}) \qquad (7)$$

$$= \Delta G_{\mathrm{form,Co,Spinel}} + \Delta G_{\mathrm{Co}} \qquad (8)$$

where $E_{\mathrm{Co}_x\mathrm{O}_y}$ and $E_{\mathrm{Co}_{x-1}\mathrm{O}_y}$ are DFT energies of the slab structures before and after the dissolution, respectively, and $E_{\mathrm{Co}}$ is the chemical potential of Co. $E_{\mathrm{Co}}$ was calculated as $0.5(E_{\mathrm{Co}_2\mathrm{O}_3} - 3E_{\mathrm{O}})$ for octahedral Co and $E_{\mathrm{CoO}} - E_{\mathrm{O}}$ for tetrahedral Co to account for the oxidation states of Co. $E_{\mathrm{Co}_2\mathrm{O}_3}$ and $E_{\mathrm{CoO}}$ are DFT energies of the most stable structures per formula unit (mp-1043418 and mp-22408), and $E_{\mathrm{O}}$ is calculated as a difference between the Gibbs free energy of $H_2O$ and $H_2$. $\Delta G_{\mathrm{form,Co,Spinel}}$ corresponds to the formation energy of the incorporation of Co in the spinel, and $\Delta G_{\mathrm{Co}}$ is the Gibbs free energy change of the standard reduction reaction of Co, which was calculated as follows:

$$\Delta G_{\mathrm{Co}} = -zFE^{\circ}_{\mathrm{Co}} + RT\ln\left(\frac{1}{[\mathrm{Co}^{z+}]}\right) \qquad (9)$$

where $z$ is the number of electrons involved, $E^{\circ}_{\mathrm{Co}}$ is the standard reduction potential of Co, $F$ is the Faraday constant, $R$ is the gas constant and $T$ is the absolute temperature, which was set to 298.15 K. $[\mathrm{Co}^{z+}]$ is the concentration of $\mathrm{Co}^{z+}$, which was assumed to be $10^{-6}$ M.[60] We note that the dissolution of Co as $\mathrm{Co}^{2+}$ was considered ($\mathrm{Co}^{2+} + 2\,e^- \rightleftharpoons \mathrm{Co}$, $E^{\circ} = -0.28$ V), which is known to be more favorable than the formation of $\mathrm{Co}^{3+}$ ($\mathrm{Co}^{3+} + 3\,e^- \rightleftharpoons \mathrm{Co}$, $E^{\circ} = +0.45$ V). The dissolution potential of Co ($U_{\mathrm{diss}}$) is given by

$$U_{\mathrm{diss}}\ (\mathrm{V_{SHE}}) = -\frac{\Delta G_{\mathrm{diss}}}{zF} \qquad (10)$$

## Data availability

All relevant data are included in the main text and its ESI.†

## Author contributions

K. L., J. S., B.-H. L., Y.-E. S., and T. H. conceived and designed the experiments. K. L. and H. J. synthesized the catalysts. K. L., J. S., H. S. L., H. J. and H. S. performed XAS characterization. J. L., W. K., M. S. B., K. K., and K.-S. L. helped with XAS and XPS data analysis. J. S., S. H., and S. Y. performed electrochemical characterizations. J. R., H. S. and H. S. L. helped with the data processing. J. K. and S. B. performed DFT calculations. K. L., J. S., H. J., B.-H. L., Y.-E. S., and T. H. co-wrote the manuscript. All authors discussed and commented on the manuscript.

## Conflicts of interest

The authors declare no competing interests.

## Acknowledgements

T. H. acknowledges the financial support by the Research Center Program of the IBS (IBS-R006-D1) in Korea. Y.-E. S. acknowledges the financial support by the IBS (IBS-R006-A2). M. S. B. acknowledges the IBS for the Young Scientist Fellowship (IBS-R006-Y2). K.-S. L. acknowledges the financial support by the National Research Foundation of Korea (2019M3D1A1079309). S. B. acknowledges the support from the National Research Foundation of Korea (NRF) funded by the Ministry of Education (NRF-2016R1A6A1A03012845) and generous supercomputing time from KISTI.

## References

1 C. Xie, Z. Niu, D. Kim, M. Li and P. Yang, *Chem. Rev.*, 2019, **120**, 1184–1249.

2 R. Qin, K. Liu, Q. Wu and N. Zheng, *Chem. Rev.*, 2020, **120**, 11810–11899.

3 N. Zhang and Y. Chai, *Energy Environ. Sci.*, 2021, **14**, 4647–4671.

4 N. Kornienko, J. Z. Zhang, K. K. Sakimoto, P. Yang and E. Reisner, *Nat. Nanotechnol.*, 2018, **13**, 890–899.

5 J. Cao, B. Wu, R. Chen, Y. Wu, Y. Hui, B. W. Mao and N. Zheng, *Adv. Mater.*, 2018, **30**, 1705596.

6 N. Tahsini, A.-C. Yang, V. Streibel, B. Werghi, E. D. Goodman, A. Aitbekova, S. R. Bare, Y. Li, F. Abild-Pedersen and M. Cargnello, *J. Am. Chem. Soc.*, 2022, **144**, 1612–1621.

7 M. H. Oh, M. G. Cho, D. Y. Chung, I. Park, Y. P. Kwon, C. Ophus, D. Kim, M. G. Kim, B. Jeong and X. W. Gu, *Nature*, 2020, **577**, 359–363.

8 Q. Zhao, Z. Yan, C. Chen and J. Chen, *Chem. Rev.*, 2017, **117**, 10121–10211.

9 J. Kim, W. Ko, J. M. Yoo, V. K. Paidi, H. Y. Jang, M. Shepit, J. Lee, H. Chang, H. S. Lee and J. Jo, *Adv. Mater.*, 2022, **34**, 2107868.

10 J. Jo, J. M. Yoo, D. H. Mok, H. Y. Jang, J. Kim, W. Ko, K. Yeom, M. S. Bootharaju, S. Back and Y.-E. Sung, *Nano Lett.*, 2022, **22**, 3636–3644.

11 M. H. Oh, T. Yu, S.-H. Yu, B. Lim, K.-T. Ko, M.-G. Willinger, D.-H. Seo, B. H. Kim, M. G. Cho and J.-H. Park, *Science*, 2013, **340**, 964–968.

12 N. Zhang, F. Cheng, Y. Liu, Q. Zhao, K. Lei, C. Chen, X. Liu and J. Chen, *J. Am. Chem. Soc.*, 2016, **138**, 12894–12901.

13 F. Cheng, J. Shen, B. Peng, Y. Pan, Z. Tao and J. Chen, *Nat. Chem.*, 2011, **3**, 79–84.

14 F. T. Haase, A. Bergmann, T. E. Jones, J. Timoshenko, A. Herzog, H. S. Jeon, C. Rettenmaier and B. R. Cuenya, *Nat. Energy*, 2022, **7**, 765–773.

15 Y. Sun, X. Ren, S. Sun, Z. Liu, S. Xi and Z. J. Xu, *Angew. Chem., Int. Ed.*, 2021, **133**, 14657–14665.

16 C. Mu, J. Mao, J. Guo, Q. Guo, Z. Li, W. Qin, Z. Hu, K. Davey, T. Ling and S. Z. Qiao, *Adv. Mater.*, 2020, **32**, 1907168.

17 Y. Jiang, Y. Zheng and S.-Z. Qiao, *Chem*, 2023, **9**, 1628–1630.

18 K.-R. Yeo, K.-S. Lee, H. Kim, J. Lee and S.-K. Kim, *Energy Environ. Sci.*, 2022, **15**, 3449–3461.

19 L. A. King, M. A. Hubert, C. Capuano, J. Manco, N. Danilovic, E. Valle, T. R. Hellstern, K. Ayers and T. F. Jaramillo, *Nat. Nanotechnol.*, 2019, **14**, 1071–1074.

20 S. Hao, H. Sheng, M. Liu, J. Huang, G. Zheng, F. Zhang, X. Liu, Z. Su, J. Hu and Y. Qian, *Nat. Nanotechnol.*, 2021, **16**, 1371–1377.

21 S. Ge, R. Xie, B. Huang, Z. Zhang, H. Liu, X. Kang, S. Hu, S. Li, Y. Luo, Q. Yu, J. Wang, G. Chai, L. Guan, H.-M. Cheng and B. Liu, *Energy Environ. Sci.*, 2023, **16**, 3734–3742.

22 H. Jin, X. Liu, P. An, C. Tang, H. Yu, Q. Zhang, H.-J. Peng, L. Gu, Y. Zheng and T. Song, *Nat. Commun.*, 2023, **14**, 354.

23 N. Danilovic, R. Subbaraman, K. C. Chang, S. H. Chang, Y. Kang, J. Snyder, A. P. Paulikas, D. Strmcnik, Y. T. Kim and D. Myers, *Angew. Chem., Int. Ed.*, 2014, **53**, 14016–14021.

24 Z.-Y. Wu, F.-Y. Chen, B. Li, S.-W. Yu, Y. Z. Finfrock, D. M. Meira, Q.-Q. Yan, P. Zhu, M.-X. Chen and T.-W. Song, *Nat. Mater.*, 2023, **22**, 100–108.

25 T. Zhu, S. Liu, B. Huang, Q. Shao, M. Wang, F. Li, X. Tan, Y. Pi, S.-C. Weng, B. Huang, Z. Hu, J. Wu, Y. Qian and X. Huang, *Energy Environ. Sci.*, 2021, **14**, 3194–3202.

26 A. Li, S. Kong, C. Guo, H. Ooka, K. Adachi, D. Hashizume, Q. Jiang, H. Han, J. Xiao and R. Nakamura, *Nat. Catal.*, 2022, **5**, 109–118.

27 J. Shan, C. Ye, S. Chen, T. Sun, Y. Jiao, L. Liu, C. Zhu, L. Song, Y. Han and M. Jaroniec, *J. Am. Chem. Soc.*, 2021, **143**, 5201–5211.

28 L. Chong, G. Gao, J. Wen, H. Li, H. Xu, Z. Green, J. D. Sugar, A. J. Kropf, W. Xu and X.-M. Lin, *Science*, 2023, **380**, 609–616.

29 F.-Y. Chen, Z.-Y. Wu, Z. Adler and H. Wang, *Joule*, 2021, **5**, 1704–1731.

30 J. Baek, M. D. Hossain, P. Mukherjee, J. Lee, K. T. Winther, J. Leem, Y. Jiang, W. C. Chueh, M. Bajdich and X. Zheng, *Nat. Commun.*, 2023, **14**, 5936.

31 C. Li, X. Han, F. Cheng, Y. Hu, C. Chen and J. Chen, *Nat. Commun.*, 2015, **6**, 7345.

32 X. Han, H. Sheng, C. Yu, T. W. Walker, G. W. Huber, J. Qiu and S. Jin, *ACS Catal.*, 2020, **10**, 6741–6752.

33 K. Chakrapani, G. Bendt, H. Hajiyani, T. Lunkenbein, M. T. Greiner, L. Masliuk, S. Salamon, J. Landers, R. Schlögl and H. Wende, *ACS Catal.*, 2018, **8**, 1259–1267.

34 M. Zhao, J. Deng, J. Liu, Y. Li, J. Liu, Z. Duan, J. Xiong, Z. Zhao, Y. Wei and W. Song, *ACS Catal.*, 2019, **9**, 7548–7567.

35 C. C. McCrory, S. Jung, J. C. Peters and T. F. Jaramillo, *J. Am. Chem. Soc.*, 2013, **135**, 16977–16987.

36 Z. W. Seh, J. Kibsgaard, C. F. Dickens, I. Chorkendorff, J. K. Nørskov and T. F. Jaramillo, *Science*, 2017, **355**, eaad4998.

37 K.-C. Kao, A.-C. Yang, W. Huang, C. Zhou, E. D. Goodman, A. Holm, C. W. Frank and M. Cargnello, *Angew. Chem., Int. Ed.*, 2021, **60**, 7971–7979.

38 A. Holm, E. D. Goodman, J. H. Stenlid, A. Aitbekova, R. Zelaya, B. T. Diroll, A. C. Johnston-Peck, K.-C. Kao, C. W. Frank, L. G. M. Pettersson and M. Cargnello, *J. Am. Chem. Soc.*, 2020, **142**, 14481–14494.

39 L. Deng, S. F. Hung, Z. Y. Lin, Y. Zhang, C. Zhang, Y. Hao, S. Liu, C. H. Kuo, H. Y. Chen and J. Peng, *Adv. Mater.*, 2023, 2305939.

40 H. Liu, Z. Zhang, J. Fang, M. Li, M. G. Sendeku, X. Wang, H. Wu, Y. Li, J. Ge and Z. Zhuang, *Joule*, 2023, **7**, 558–573.

41 W. Jing, H. Shen, R. Qin, Q. Wu, K. Liu and N. Zheng, *Chem. Rev.*, 2022, **123**, 5948–6002.

42 A. Aitbekova, C. Zhou, M. L. Stone, J. S. Lezama-Pacheco, A.-C. Yang, A. S. Hoffman, E. D. Goodman, P. Huber, J. F. Stebbins, K. C. Bustillo, P. Ercius, J. Ciston, S. R. Bare, P. N. Plessow and M. Cargnello, *Nat. Mater.*, 2022, **21**, 1290–1297.

43 S. Yamazoe, Y. Hitomi, T. Shishido and T. Tanaka, *J. Phys. Chem. C*, 2008, **112**, 6869–6879.

44 J. Peng, B. Chen, Z. Wang, J. Guo, B. Wu, S. Hao, Q. Zhang, L. Gu, Q. Zhou and Z. Liu, *Nature*, 2020, **586**, 390–394.

45 D. Lu, Y. Zhang, M. Lai, A. Lee, C. Xie, J. Lin, T. Lei, Z. Lin, C. S. Kley and J. Huang, *Nano Lett.*, 2018, **18**, 6967–6973.

46 Z. Liu, G. Wang, X. Zhu, Y. Wang, Y. Zou, S. Zang and S. Wang, *Angew. Chem., Int. Ed.*, 2020, **132**, 4766–4772.

47 W. Qu, Z. Tang, S. Tang, H. Wen, J. Fang, Q. Lian, D. Shu and C. He, *Adv. Funct. Mater.*, 2023, **33**, 2301677.

48 D. Y. Chung, P. P. Lopes, P. Farinazzo Bergamo Dias Martins, H. He, T. Kawaguchi, P. Zapol, H. You, D. Tripkovic, D. Strmcnik and Y. Zhu, *Nat. Energy*, 2020, **5**, 222–230.

49 M. Kim, J. Park, H. Ju, J. Y. Kim, H.-S. Cho, C.-H. Kim, B.-H. Kim and S. W. Lee, *Energy Environ. Sci.*, 2021, **14**, 3053–3063.

50 G. Kresse and J. Furthmüller, *Phys. Rev. B: Condens. Matter Mater. Phys.*, 1996, **54**, 11169.

51 G. Kresse and J. Furthmüller, *Comput. Mater. Sci.*, 1996, **6**, 15–50.

52 P. E. Blöchl, *Phys. Rev. B: Condens. Matter Mater. Phys.*, 1994, **50**, 17953.

53 G. Kresse and D. Joubert, *Phys. Rev. B: Condens. Matter Mater. Phys.*, 1999, **59**, 1758.

54 J. P. Perdew, K. Burke and M. Ernzerhof, *Phys. Rev. Lett.*, 1996, **77**, 3865.

55 S. L. Dudarev, G. A. Botton, S. Y. Savrasov, C. Humphreys and A. P. Sutton, *Phys. Rev. B: Condens. Matter Mater. Phys.*, 1998, **57**, 1505.

56 H. J. Monkhorst and J. D. Pack, *Phys. Rev. B: Condens. Matter Mater. Phys.*, 1976, **13**, 5188.

57 J. K. Nørskov, J. Rossmeisl, A. Logadottir, L. Lindqvist, J. R. Kitchin, T. Bligaard and H. Jonsson, *J. Phys. Chem. B*, 2004, **108**, 17886–17892.

58 J. Rossmeisl, Z.-W. Qu, H. Zhu, G.-J. Kroes and J. K. Nørskov, *J. Electroanal. Chem.*, 2007, **607**, 83–89.

59 A. H. Larsen, J. J. Mortensen, J. Blomqvist, I. E. Castelli, R. Christensen, M. Dułak, J. Friis, M. N. Groves, B. Hammer and C. Hargus, *J. Phys.: Condens. Matter*, 2017, **29**, 273002.

60 K. A. Persson, B. Waldwick, P. Lazic and G. Ceder, *Phys. Rev. B: Condens. Matter Mater. Phys.*, 2012, **85**, 235438.